arXiv:1703.07222v1 [cond-mat.quant-gas] 21 Mar 2017

Quantum Hall phase diagram of two-component Bose gases: Intercomponent entanglement and pseudopotentials

Shunsuke Furukawa[1] and Masahito Ueda[1,2]

[1]*Department of Physics, University of Tokyo, 7-3-1 Hongo, Bunkyo-ku, Tokyo 113-0033, Japan*
[2]*RIKEN Center for Emergent Matter Science (CEMS), Wako, Saitama 351-0198, Japan*

(Dated: March 22, 2017)

We study the ground-state phase diagram of two-dimensional two-component (or pseudospin-$\frac{1}{2}$) Bose gases in a high synthetic magnetic field in the space of the total filling factor and the ratio of the intercomponent coupling $g_{\uparrow\downarrow}$ to the intracomponent one $g > 0$. Using exact diagonalization, we find that when the intercomponent coupling is attractive ($g_{\uparrow\downarrow} < 0$), the product states of a pair of nearly uncorrelated quantum Hall states are remarkably robust and persist even when $|g_{\uparrow\downarrow}|$ is close to g. This contrasts with the case of an intercomponent repulsion, where a variety of spin-singlet quantum Hall states with high intercomponent entanglement emerge for $g_{\uparrow\downarrow} \approx g$. We interpret this marked dependence on the sign of $g_{\uparrow\downarrow}$ in light of pseudopotentials on a sphere, and also explain recent numerical results in two-component Bose gases in mutually antiparallel magnetic fields where a qualitatively opposite dependence on the sign of $g_{\uparrow\downarrow}$ is found. Our results thus unveil an intriguing connection between multicomponent quantum Hall systems and quantum spin Hall systems in minimal setups.

PACS numbers: 05.30.Jp, 03.75.Mn, 67.85.Fg, 73.43.Cd

I. INTRODUCTION

Engineering synthetic gauge fields in ultracold atomic systems has been a subject of active interest recently [1, 2]. While a real magnetic field does not produce a Lorentz force for neutral atoms, different methods of creating synthetic magnetic fields that do produce such a force have been developed. Such methods include rotation [3–6] and optical dressing [7] of atoms in continuum and laser-induced tunneling in optical lattices in real [8–10] and synthetic [11–13] spaces. For two-component (or pseudospin-$\frac{1}{2}$) gases, which are populated in two hyperfine spin states of the same atomic species, a richer variety of gauge fields have been created, such as a uniform magnetic field by rotation [14, 15], and spin-orbit couplings [16–21] and pseudospin-dependent antiparallel magnetic fields [22] by optical dressing techniques. By using these techniques, we can expect to emulate quantum Hall (QH) states and other topological states of matter in highly controlled atomic systems and to explore many-body phenomena beyond the scope of other condensed matter systems [23, 24]. The capability to prepare bosonic particles in gauge fields is particularly unique to atomic systems. For moderate synthetic magnetic fields, a scalar Bose-Einstein condensate exhibits Abrikosov's triangular vortex lattice as observed experimentally [4, 5]. For high synthetic fields, theory predicts that the vortex lattice melts and that incompressible QH states appear at various integer and fractional values of the filling factor $\nu = N/N_\phi$, where N is the number of atoms and N_ϕ is the number of flux quanta piercing the system [6]. Such QH states of scalar bosons include a bosonic Laughlin state at $\nu = 1/2$ [25, 26], Jain's composite fermion (CF) states at $\nu = p/(p+1)$ ($p = 2, 3, \dots$) [27–29], and a non-Abelian Moore-Read state at $\nu = 1$ [30, 31]. The Laughlin and Moore-Read states are two members of the Read-Rezayi series of states with an $\mathrm{SU}(2)_k$ symmetry at $\nu = k/2$ ($k = 1, 2, \dots$) [32].

A large number of theoretical studies have recently been conducted for two-dimensional (2D) pseudospin-$\frac{1}{2}$ Bose gases in a uniform synthetic magnetic field, where richer physics than the scalar case is naturally expected. We introduce the total filling factor $\nu = (N_\uparrow + N_\downarrow)/N_\phi$, where $N_\uparrow$ and $N_\downarrow$ are the numbers of pseudospin-$\uparrow$ and $\downarrow$ bosons, respectively. Within the Gross-Pitaevskii mean field theory which is valid for $\nu \gg 1$, several different types of vortex lattices have been shown to appear as the ratio of the intercomponent contact interaction $g_{\uparrow\downarrow}$ to the intracomponent one $g > 0$ is varied [33, 34]. Meanwhile, studies on a high-magnetic-field regime with $\nu = O(1)$ have revealed that various spin-singlet QH states emerge for pseudospin-independent (SU(2)-symmetric) interactions with $g_{\uparrow\downarrow} = g > 0$. Examples are the Halperin (221) state with an $\mathrm{SU}(3)_1$ symmetry at $\nu = 2/3$ [35, 36], a non-Abelian $\mathrm{SU}(3)_2$ state at $\nu = 4/3$ [37–40], and a bosonic integer QH (BIQH) state protected by a $U(1)$ symmetry at $\nu = 2$ [41–46] (similar states have also been shown to appear in interacting scalar bosons in topological flat bands with Chern number two [47–54] and a correlated honeycomb lattice model [55]). Furthermore, a gapless spin-singlet composite Fermi liquid (CFL) has been shown to appear at $\nu = 1$ [56]. In all these states, the two components are highly entangled. For small $|g_{\uparrow\downarrow}|/g$, in contrast, the system can be viewed as two weakly coupled scalar Bose gases, and the product states of nearly independent QH states (referred to as *doubled* QH states hereafter) are expected to appear. It is thus interesting to investigate the phase diagram with varying $g_{\uparrow\downarrow}/g$ and analyze the competition among various QH states.

In this paper, we determine the ground-state (GS) phase diagram of pseudospin-$\frac{1}{2}$ Bose gases in a uniform

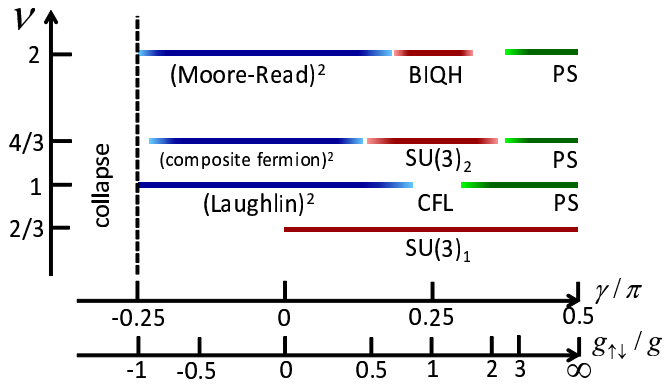

FIG. 1: (color online) GS phase diagram in the space of the total filling factor ν and the ratio $g_{\uparrow\downarrow}/g = \tan\gamma$ of the intercomponent to intracomponent coupling constants. We assume an intracomponent repulsion $g > 0$. For an intercomponent attraction $g_{\uparrow\downarrow} < 0$, the product states of a pair of nearly uncorrelated QH states (Laughlin, CF, and Moore-Read states) are found to appear over wide ranges of $g_{\uparrow\downarrow}/g$. For $g_{\uparrow\downarrow} \approx g$, in contrast, a variety of spin-singlet QH states with high intercomponent entanglement appear, such as the $SU(2)_k$ states at $\nu = 2k/3$ ($k = 1, 2$) [35–40] and a BIQH state at $\nu = 2$ [41–46] (for $\nu = 4/3$, a different scenario in favor of a composite fermion spin-singlet state has been given in Ref. [43]). Furthermore, a gapless spin-singlet CFL appears at $\nu = 1$ [56]. For larger $g_{\uparrow\downarrow}/g$, a phase separation (PS) occurs. The ranges of different phases indicated by shaded bars are determined in Sec. II, and may contain errors due to finite-size effects or ambiguity in setting the condition for detecting the phase boundaries.

synthetic magnetic field in the space of the total filling factor ν and the coupling ratio $g_{\uparrow\downarrow}/g$. To this end, we have performed an extensive exact diagonalization analysis in the lowest-Landau-level (LLL) basis on spherical and torus geometries. Our main results are summarized in Fig. 1. Here we parametrize the two coupling constants as

$$(g, g_{\uparrow\downarrow}) = G\ell^2(\cos\gamma, \sin\gamma) \tag{1}$$

with $G > 0$, and change γ in the range $-\pi/2 \le \gamma \le \pi/2$. As seen in this diagram, when the intercomponent coupling is attractive ($g_{\uparrow\downarrow} < 0$), doubled QH states are remarkably robust and persist even when $|g_{\uparrow\downarrow}|$ is comparable to the intracomponent coupling $g > 0$. This sharply contrasts with the case of an intercomponent repulsion ($g_{\uparrow\downarrow} > 0$), where a variety of spin-singlet QH states with high intercomponent entanglement emerge for $g_{\uparrow\downarrow} \approx g$. We interpret this remarkable dependence on the sign of $g_{\uparrow\downarrow}$ in light of Haldane's pseudopotentials on a sphere [57, 58]. More specifically, the stability of the doubled QH states for $g_{\uparrow\downarrow} < 0$ can be understood from the "ferromagnetic" nature of the intercomponent interaction in terms of (modified) angular momenta of the particles. We note that some previous numerical works also investigated the phase diagram in the space of the coupling ratio $g_{\uparrow\downarrow}/g$ for $\nu = 1$ [59], $\nu = 4/3$ [40], and $\nu = 2$ [44]. However, since these works set different conditions in determining the phase boundaries and might involve finite-size effects in different manners, it is worthwhile to reexamine the phase diagrams at these filling factors in a comparative manner along the same line of analyses. Furthermore, the case of $g_{\uparrow\downarrow} < 0$ was not analyzed in these works.

It is interesting to compare Fig. 1 with the phase diagram of two-component Bose gases in *antiparallel* magnetic fields studied previously [60] (see also Refs. [61, 62] for earlier studies on the same and related systems). In the latter case, the pseudospin-$\uparrow$ ($\downarrow$) component is subject to the magnetic field $+B$ ($-B$) in the direction perpendicular to the 2D gas, and the system possesses the time-reversal symmetry. Within the Gross-Pitaevskii mean-field theory which is valid for $\nu \gg 1$, one can show that the system in antiparallel fields shows the same vortex structures as the system in parallel fields studied in Refs. [33, 34]. However, a remarkable distinction emerges in a high-field regime with $\nu = O(1)$: in the case of antiparallel fields, (fractional) quantum spin Hall states [63] composed of a pair of QH states with opposite chiralities are robust for an intercomponent repulsion $g_{\uparrow\downarrow} > 0$ and persist for $g_{\uparrow\downarrow}$ as large as g. Similar results have also been found in the stability of two coupled bosonic Laughlin states in lattice models [64]. These results suggest that the case of $g_{\uparrow\downarrow} > 0$ for antiparallel fields essentially corresponds to the case of $g_{\uparrow\downarrow} < 0$ for parallel fields. As discussed later, the pseudopotential approach also provides an understanding of this intriguing correspondence.

The rest of the paper is organized as follows. In Sec. II, we present our exact diagonalization results. In particular, we perform an extensive search for incompressible states in the present system, and determine the parameter ranges of different QH states shown in Fig. 1. In Sec. III, we discuss the stability of coupled QH states in light of pseudopotentials on a sphere. In Sec. IV, we present a summary and an outlook for future studies. In Appendix A, we summarize QH wave functions discussed in the paper. In Appendix B, we describe some details on the calculation of pseudopotentials for two-component gases in antiparallel fields.

II. EXACT DIAGONALIZATION ANALYSIS

In this section, we present our exact diagonalization analysis that has led to the phase diagram in Fig. 1. We consider a system of a 2D pseudospin-$\frac{1}{2}$ Bose gas (in the xy plane) having two hyperfine spin states (labeled by $\alpha = \uparrow, \downarrow$) and subject to a synthetic magnetic field B along the z axis. In the case of a rotating gas, the field $B = 2M\Omega/q$ is induced in the rotating frame of reference, where M and q are the mass and the fictitious charge, respectively, of a neutral atom and Ω is the rotation frequency. We denote the strengths of the intracomponent and intercomponent contact interactions

by g and $g_{\uparrow\downarrow}$, respectively. In the second-quantized form, the interaction Hamiltonian is written as

$$H_{\rm int} = \sum_{\alpha,\beta=\uparrow,\downarrow} \frac{g_{\alpha\beta}}{2} \int d^2\boldsymbol{r} \hat{\Psi}^\dagger_\alpha(\boldsymbol{r}) \hat{\Psi}^\dagger_\beta(\boldsymbol{r}) \hat{\Psi}_\beta(\boldsymbol{r}) \hat{\Psi}_\alpha(\boldsymbol{r}), \quad (2)$$

where $\hat{\Psi}_\alpha(\boldsymbol{r})$ is the bosonic field operator for the spin state α. We set $g_{\uparrow\uparrow} = g_{\downarrow\downarrow} \equiv g > 0$ and $g_{\uparrow\downarrow} = g_{\downarrow\uparrow}$. For a 2D system of area A, the number of magnetic flux quanta piercing the system is given by $N_\phi = A/(2\pi\ell^2)$, where $\ell = \sqrt{\hbar/|qB|}$ is the magnetic length. Strongly correlated physics is expected to emerge when N_ϕ becomes comparable with or larger than the total number of particles, $N = N_\uparrow + N_\downarrow$, for sufficiently high B. For such high B, it is useful to restrict ourselves to the low-energy subspace spanned by the LLL states. Within this restricted subspace, we have performed an exact diagonalization analysis of the interaction Hamiltonian (2). Our analysis presented here is quite analogous to the one performed for the systems in antiparallel fields in Ref. [60].

A. Spherical and torus geometries

To study bulk properties, it is useful to work on closed uniform manifolds having no edge. In our analysis, we employ spherical [57, 58] and torus [65, 66] geometries as was done in previous studies on the same and related systems [38–40, 42–44, 46, 56, 59, 67, 68]. These geometries can describe the central region of a trapped gas, where the particle density is approximately uniform. Here we briefly describe the basic features of these geometries.

For a spherical geometry, a magnetic monopole of charge $-N_\phi(2\pi\hbar/q)$ with integer $N_\phi \equiv 2S$ is placed at the origin. It produces a uniform magnetic field $-B$ on the sphere of radius $R = \ell\sqrt{S}$. The LLL on a sphere corresponds to the subspace in which a certain modified angular momentum [as shown in Eq. (B1) in Appendix B] has the magnitude S, and is thus $(2S+1)$-fold degenerate. Introducing the spherical coordinates (θ, φ) and the spinor coordinates

$$u = \cos(\theta/2)e^{i\phi/2}, \; v = \sin(\theta/2)e^{-i\phi/2}, \quad (3)$$

single-particle orbitals in the LLL are given by $\psi_m \propto u^{S+m}v^{S-m}$, where $m \in \{-S, -S+1, \ldots, S\}$ is the z-component of the angular momentum. On a sphere, the interaction Hamiltonian (2) in the LLL subspace can conveniently be represented in terms of pseudopotentials [57, 58], as explained in Sec. III. Because of the spherical symmetry, many-body eigenstates can be classified by the total angular momentum L.

A torus geometry is formed by a periodic rectangle of sides L_x and L_y. The degeneracy in the LLL manifold is given by $N_\phi = L_xL_y/(2\pi\ell^2)$. In our analysis, we set $L_x = L_y$. The representation of the interaction Hamiltonian (2) in the LLL basis on this geometry can be found in, e.g., Ref. [46]. The many-body eigenstates can be classified by the total pseudomomentum $\boldsymbol{K} = (K_x, K_y) = 2\pi\hbar(m_x/L_x, m_y/L_y)$. When $(N_\phi, N) = (q, p)\bar{N}$ with $\bar{N}$ being the largest common divisor of N_ϕ and N, the two integers m_x and m_y can take $m_x \in \{0, 1, \ldots, q\bar{N}-1\}$ and $m_y \in \{0, 1, \ldots, \bar{N}-1\}$. Since eigenstates with m_x and $m_x + \bar{N}$ are related by a translation in the y direction, all the eigenenergies are q-fold degenerate [66].

On both the sphere and the torus, the filling factor in the thermodynamic limit is given by $\nu = N/N_\phi$. For incompressible states on finite spheres, however, the relation between N and N_ϕ involves a characteristic shift δ as follows:

$$N = \nu(N_\phi + \delta), \quad (4)$$

where δ depends on individual candidate wave functions. Therefore, on a sphere, competing incompressible states leading to the same ν in the thermodynamic limit can be studied separately with different (N_ϕ, N) if they have different shifts. On a torus, there is no shift, and all candidates for the same ν compete in the same finite-size calculation.

B. Numerical search for incompressible states

Through exact diagonalization calculations on a spherical geometry, we have carried out an extensive search for incompressible GSs in the (N_ϕ, N) plane for different values of $\gamma = \arctan(g_{\uparrow\downarrow}/g)$ as shown in Fig. 2. Incompressible states in general appear as the unique GSs with $L = 0$, which are indicated by filled circles. The area of each filled circle is proportional to the neutral gap Δ_n (in units of G), which is defined as the excitation gap for fixed $(N_\phi, N_\uparrow, N_\downarrow)$. Five types of lines indicate the relation (4) for different candidate QH states; see Appendix A for the wave functions of these states.

For small γ, doubled QH states are expected to appear. In Fig. 2, solid lines correspond to the doubled Read-Rezayi $\mathrm{SU}(2)_k$ states at $\nu = k$ $(k = 1, 2, 3, 4)$, which include the doubled Laughlin $(k = 1)$ and Moore-Read $(k = 2)$ states (we note that these states appear only for even N_ϕ). Dashed dotted lines correspond to doubled CF states at $\nu = \frac{2p}{p+1}$ $(p = 2, 3)$. For (a) $\gamma = -0.1\pi$ and (b) $\gamma = 0.05\pi$, we find that $L = 0$ GSs appear on these lines with relatively large excitation gaps Δ_n/G for $\nu = 1$, 4/3, and 2. For $-\pi/2 \lesssim \gamma \leq 0$ (i.e., $-1 \lesssim g_{\uparrow\downarrow} \leq 0$), we find that $L = 0$ GSs continue to appear on these lines although the gaps Δ_n/G gradually shrink with increasing $|\gamma|$. In contrast, as we increase γ in $0 \leq \gamma < \pi/4$, some of the GSs on these lines are replaced by $L > 0$ states, as seen for (c) $\gamma = 0.2\pi$. These results suggest that the doubled QH states are more stable for $\gamma < 0$.

At $\gamma = \pi/4$ (i.e., $g_{\uparrow\downarrow} = g$), the system possesses the SU(2) spin rotational symmetry, and a variety of spin-singlet QH states appear as revealed in previous studies. Such spin-singlet QH states include the $\mathrm{SU}(3)_k$ states

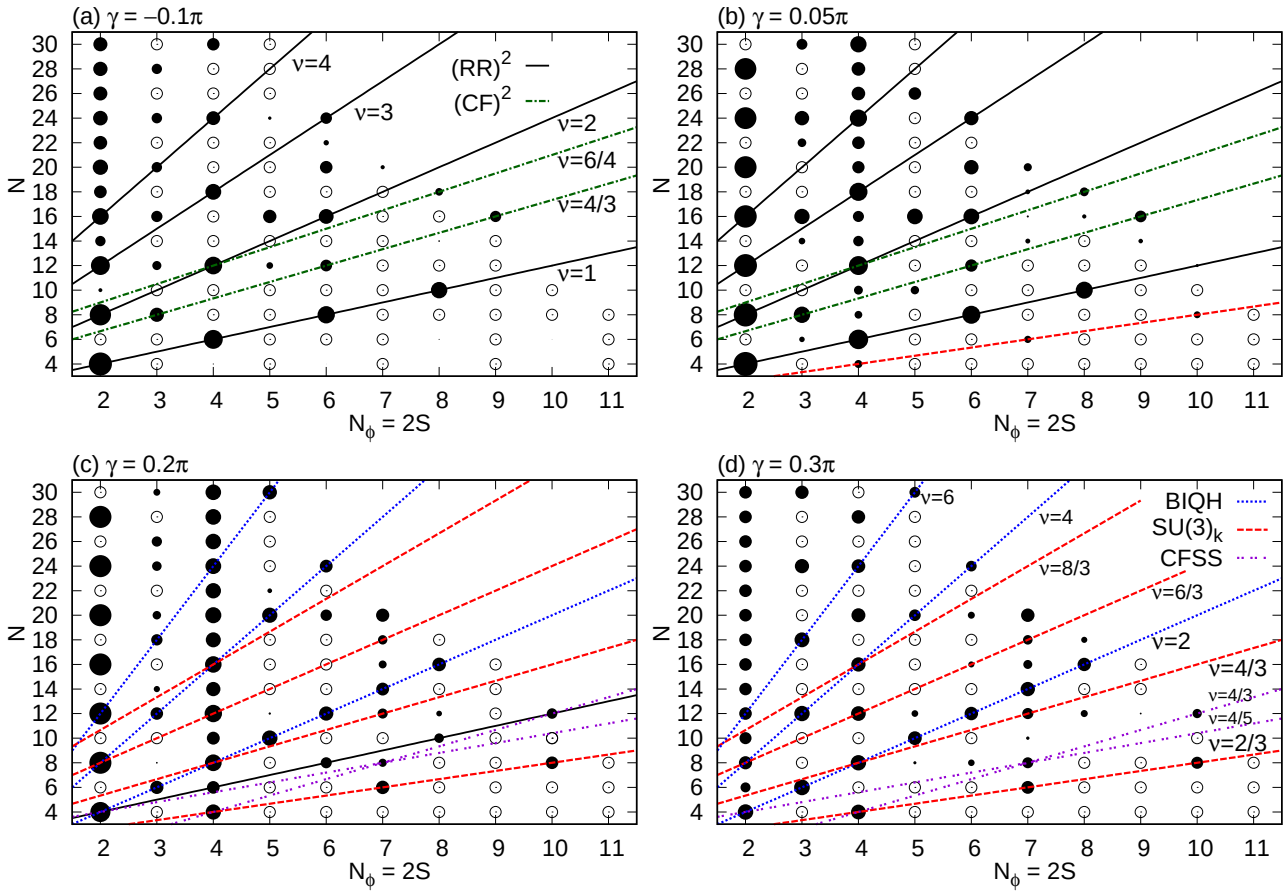

FIG. 2: (color online) Candidates for incompressible GSs in the (N_ϕ, N) plane, calculated on a spherical geometry for different values of $\gamma = \arctan(g_{\uparrow\downarrow}/g)$. Filled circles indicate GSs with the total angular momentum $L = 0$, where incompressible states can appear; the area of each filled circle is proportional to the neutral gap Δ_n/G. Empty circles indicate the GSs with $L > 0$. Five types of lines indicate the relation (4) for different QH states: the doubled Read-Rezayi $SU(2)_k$ states $[(\nu, \delta) = (k, 2)$; black solid], the doubled CF states $[(\nu, \delta) = (\frac{2p}{p+1}, p+1)$; green dashed dotted], the $SU(3)_k$ states $[(\nu, \delta) = (\frac{2k}{3}, 2)$; red dashed], the BIQH state (with its possible generalizations) $[(\nu, \delta) = (2k, 0)$; blue dotted], and the CFSS states $[(\nu, \delta) = (\frac{4}{5}, 3), (\frac{4}{3}, -1)$; purple double dotted]. Data points are missing for large N_ϕ or N due to an exponentially increasing computation time.

at $\nu = 2k/3$ [35–40], the BIQH states at $\nu = 2$ [41–44] (with possible generalizations to $\nu = 4, 6, \ldots$ [42]), and CF spin-singlet (CFSS) states at $\nu = 4/5$ and $4/3$ [43]. Since these states have finite excitation gaps, they are expected to be stable over some ranges around the SU(2) case. For (c) $\gamma = 0.2\pi$ and (d) $\gamma = 0.3\pi$ in Fig. 2, $L = 0$ GSs are indeed found on the lines corresponding to these states (for a similar plot in the SU(2) case $\gamma = \pi/4$, see Ref. [42]). In particular, large gaps are found for the $SU(3)_1$ state at $\nu = 2/3$ and the BIQH state at $\nu = 2$. At $\nu = 2/3$, the $SU(3)_1$ state (Halperin (221) state) is known to be the exact zero-energy GS for repulsive contact interactions $g, g_{\uparrow\downarrow} > 0$ [36]. Although the BIQH and $SU(3)_3$ states compete at $\nu = 2$, the gap for the former is (by a factor of about 1.5) larger than that for the latter, indicating that the BIQH state is likely to survive the competition [42]. At $\nu = 4/3$, the $SU(3)_2$ and CFSS states compete; although the gap values for these states are close, the gap for the $SU(3)_2$ state is slightly larger [42].

This section has focused on a global picture of the types and the ranges of incompressible states present in the system. More precise estimation of the parameter range of each QH phase requires a more detailed analysis, which we present next.

C. Parameter ranges of quantum Hall states

Hereafter we focus on the filing factors $\nu = 2/3$, 1, 4/3, and 2, where the QH states have relatively large excitation gaps. We determine the parameter ranges of the QH phases which are identified in Sec. II B.

Similar to Ref. [60], we examine two kinds of quantities for this purpose: the fidelity susceptibility and the squared overlap of the GS with representative wave func-

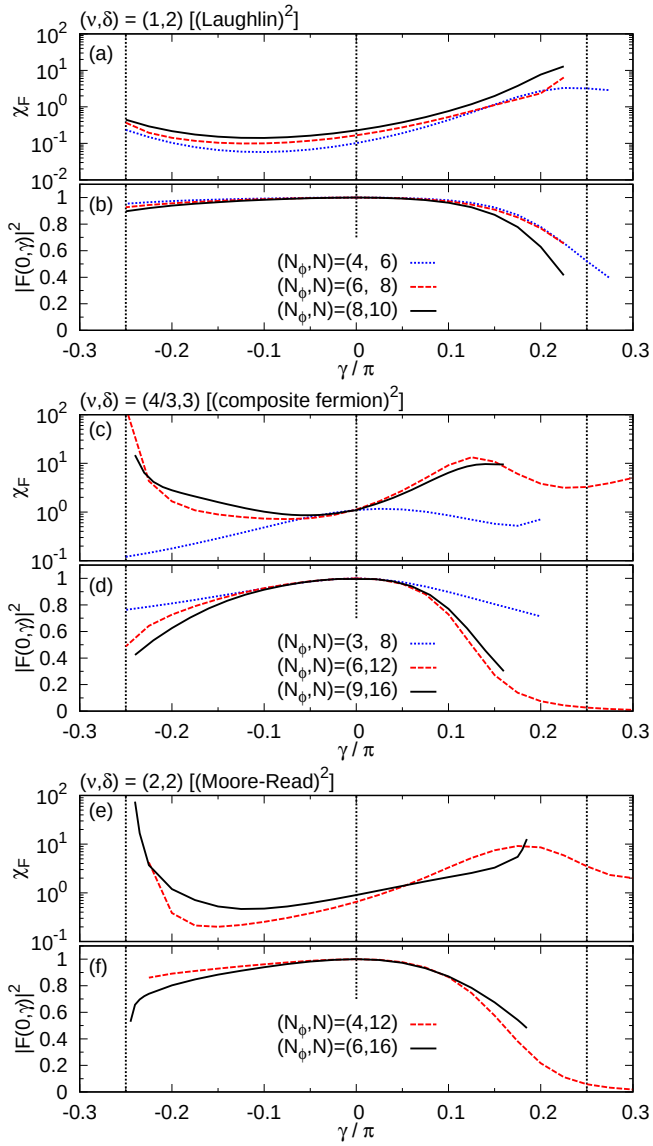

FIG. 3: (color online) (a,c,e) The fidelity susceptibility $\chi_F(\gamma)$ and (b,d,f) the squared overlap $|F(0,\gamma)|^2$ with the decoupled case as functions of γ. Calculations are performed on a spherical geometry for $\nu = 1$, 4/3, and 2. Curves are shown in the regions where the GS remains in the same sector. Vertical dotted lines correspond to $\gamma = 0, \pm\pi/4$.

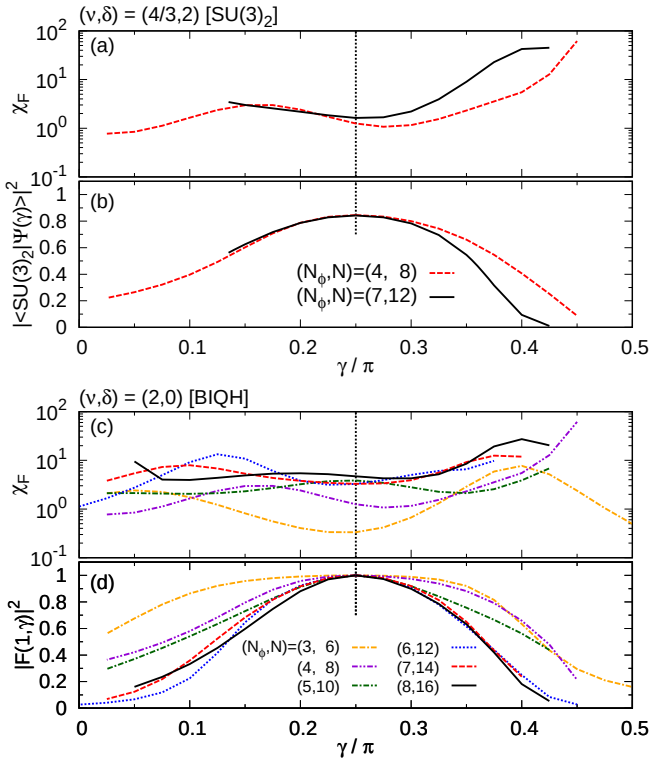

FIG. 4: (color online) (a,c) The fidelity susceptibility $\chi_F(\gamma)$, (b) the squared overlap with the $SU(3)_2$ wave function, and (d) the squared overlap $|F(1,\gamma)|^2$ with the SU(2) case, as functions of γ around $\gamma = \pi/4$ (the vertical dotted lines). Calculations are performed on a spherical geometry. Curves are shown in the regions where the GS remains in the same sector. The values at $\gamma = \pi/4$ in (b) are consistent with Ref. [43].

tions. The fidelity susceptibility χ_F measures how fast the GS changes as a function of γ, and is defined as [69]

$$\chi_F(\gamma) = -2 \lim_{\delta\gamma\to 0} \frac{\ln F(\gamma, \gamma+\delta\gamma)}{(\delta\gamma)^2}, \qquad (5)$$

where $F(\gamma, \gamma+\delta\gamma) = |\langle\Psi(\gamma)|\Psi(\gamma+\delta\gamma)\rangle|$ is the overlap between the GSs at two close points γ and $\gamma+\delta\gamma$. A peak in this quantity in general signals a phase transition. This quantity turned out to be quite useful for detecting phase transitions in the case of antiparallel fields [60]. In the present case of parallel fields, however, χ_F does not show a clear peak structure or a smooth dependence on the system size; this may be attributed to severer finite-size effects due to more complicated competition among various QH states. Thus we mainly use the squared overlap of the GS with representative wave functions in the estimation of phase boundaries.

In Fig. 3, we analyze the parameter ranges of the doubled QH states. In the decoupled case ($\gamma = 0$), the GS for $(\nu, \delta) = (1, 2)$ is given exactly by the doubled Laughlin wave functions [26]. At the same point, the GSs for $(\nu, \delta) = (4/3, 3)$ and $(2, 2)$ have large overlaps with the doubled CF wave functions and the doubled Moore-Read wave functions, respectively; indeed, the squared overlaps with these wave functions are 0.98^2 and 0.96687^2 for $(N_\phi, N) = (9, 16)$ and $(6, 16)$, respectively [29], where the square comes from the presence of two components. In Fig. 3(b,d,f), we plot the squared overlap $|F(0,\gamma)|^2$ of the GS with the decoupled case to analyze the stability of these doubled QH states. We find that $|F(0,\gamma)|^2$ decreases more slowly for $\gamma < 0$ than for $\gamma > 0$ as we move away from the decoupled case; this indicates that the doubled QH states are more robust for an intercompo-

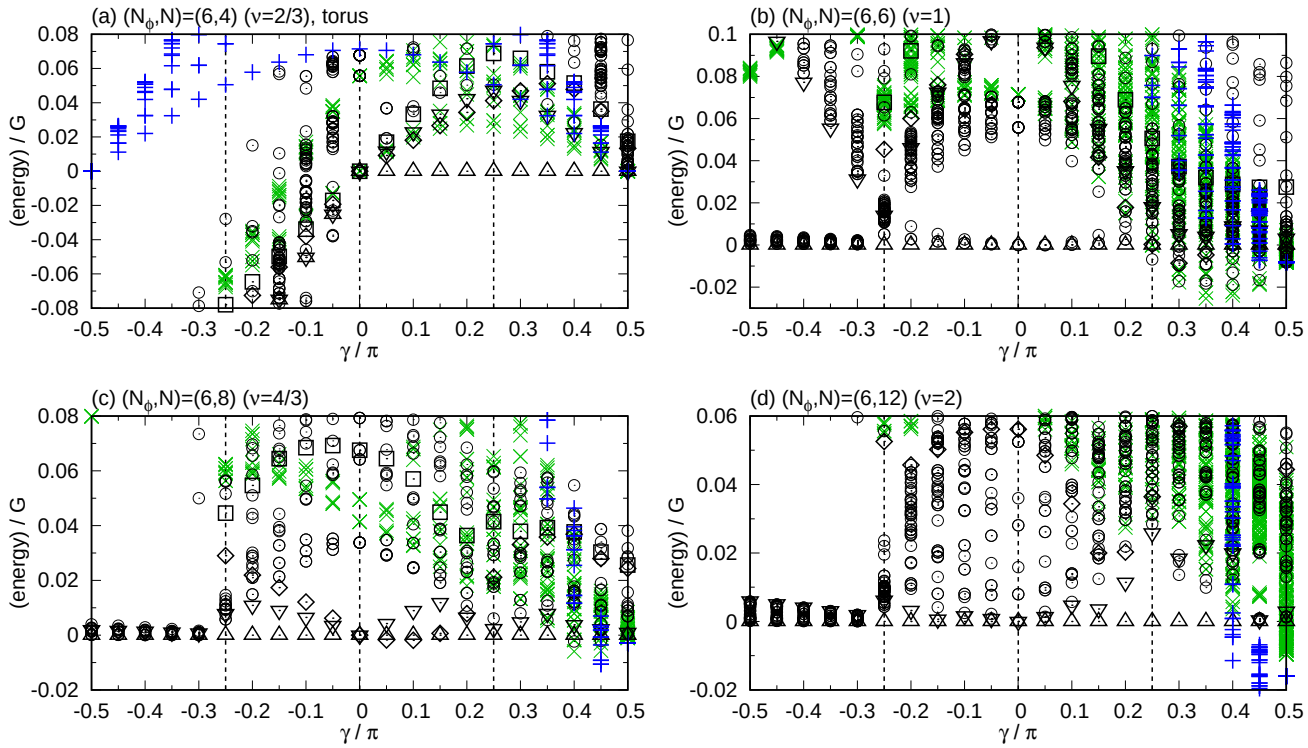

FIG. 5: (color online) Energy spectra versus γ for $\nu = 2/3$, 1, 4/3, and 2 with $N_\phi = 6$ on a torus geometry. The eigenstates are classified by the magnetization (or population imbalance) $S_z = (N_\uparrow - N_\downarrow)/2$ and the pseudomomentum $\boldsymbol{K}$. Upward ($\triangle$) and downward ($\triangledown$) triangles indicate the two lowest-energy states in the sector with $\boldsymbol{K} = \boldsymbol{0}$ and $\rho_\pi = p_{\uparrow\downarrow} = +1$ in the equal-population case $S_z = 0$, where ρ_π and $p_{\uparrow\downarrow}$ are the quantum numbers associated with the π spatial rotation and the interchange of the two components, respectively. The lowest energy in this sector is subtracted from the entire spectrum in (b,c,d). Diamonds ($\diamond$) and squares ($\square$) indicate the two lowest-energy states in the sector with $\boldsymbol{K} = \boldsymbol{0}$ and $\rho_\pi = p_{\uparrow\downarrow} = -1$. Circles ($\bigcirc$) indicate other eigenstates in the equal-population case. Greek (+) and diagonal ($\times$) crosses indicate eigenstates in the fully ($S_z = \pm N/2$) and partially ($0 < |S_z| < N/2$) imbalanced cases, respectively. Only the two lowest energies are displayed in each sector. For $\nu = p/q$ (with p and q being coprime), each eigenenergy is q-fold degenerate.

nent attraction $g_{\uparrow\downarrow} < 0$. In general, the squared overlap can only show a smooth behavior across a phase transition point in finite-size systems (unless the GS moves to another sector); furthermore, it tends to decrease exponentially with the system size owing to an exponentially increasing Hilbert space dimension. To estimate the parameter ranges of the doubled QH states from the present data, a useful guidance can be gained from Ref. [60]: in the case of antiparallel fields, a peak in the fidelity susceptibility χ_F is found when the squared overlap $|F(0,\gamma)|^2$ is around 0.5 for the largest system size treated in each of Fig. 3(b,d,f). Using the data for such system sizes and finding the points where $|F(0,\gamma)|^2$ becomes 0.5 or the GS moves to another sector, we can estimate the ranges of the doubled QH states as follows

$$\begin{aligned} (\text{Laughlin})^2 &: -0.25\pi < \gamma \lesssim 0.22\pi, \\ (\text{composite fermion})^2 &: -0.23\pi \lesssim \gamma \lesssim 0.13\pi, \\ (\text{Moore-Read})^2 &: -0.25\pi \lesssim \gamma \lesssim 0.18\pi. \end{aligned} \quad (6)$$

Around the boundaries of these ranges, χ_F shows peaks or takes relatively large values as seen in Fig. 3(a,c,e). We note that the above estimates can contain errors due to finite-size effects or ambiguity in setting the condition for $|F(0,\gamma)|^2$. A more precise determination of phase boundaries requires a simulation in larger systems by using, e.g., the density matrix renormalization group [70–72].

We have performed a similar analysis to estimate the ranges of the spin-singlet QH states as shown in Fig. 4. In Fig. 4(b), we examine the squared overlap of the GS with the SU(3)$_2$ wave function for $(\nu, \delta) = (4/3, 2)$; the latter is constructed by calculating the GS for the 3-body contact interaction [see Eq. (A5) in Appendix A]. Finding the points where $|\langle \mathrm{SU(3)}_2|\Psi(\gamma)\rangle|^2 = 0.5$ or the GS sector changes in the data for $(N_\phi, N) = (7, 12)$, we estimate the range of the SU(3)$_2$ state to be $0.14\pi \lesssim \gamma \lesssim 0.36\pi$. In Fig. 4(d), we examine the squared overlap $|F(1,\gamma)|^2$ with the SU(2) case for $(\nu, \delta) = (2, 0)$ to analyze the range of the BIQH state. We note that the squared overlap between our reference state $|\Psi(1)\rangle$ and the BIQH wave function is 0.789 for $(N_\phi, N) = (7, 14)$ [43]. The condition $|F(1,\gamma)|^2 = 0.5$ leads to the range $0.13\pi \lesssim \gamma \lesssim 0.37\pi$,

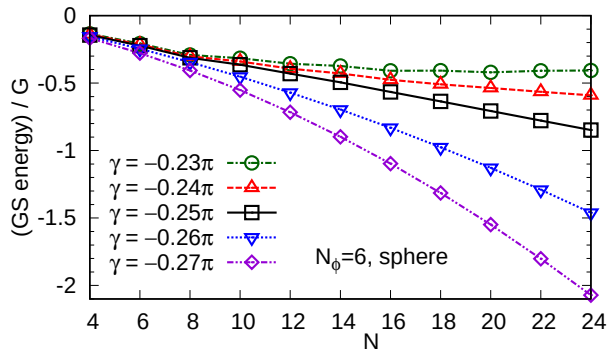

FIG. 6: (color online) GS energy as a function of N for different values of γ around $-\pi/4$. We use a spherical geometry and set $N_\phi = 6$.

which overlaps with the estimated range of the doubled Moore-Read states in Eq. (6). Since the overlap between $|\Psi(1)\rangle$ and the BIQH wave function is not perfect, we need a stricter condition. With the condition $|F(1,\gamma)|^2 = 0.8$, for example, we can estimate the range of the BIQH state to be $0.18\pi \lesssim \gamma \lesssim 0.32\pi$. An even stricter condition was used in Ref. [44].

Finally, we examine energy spectra on a torus geometry in Fig. 5. A torus geometry can provide less biased results since there is no shift and different candidates of QH states can compete in the same finite-size calculation. However, the presence of topological degeneracy can make the analysis more complex. For $\nu = 2/3$ in Fig. 5(a), we can clearly see the presence of a gap above the zero-energy $SU(3)_1$ state (with 3-fold degeneracy) for $0 < \gamma < \pi/2$. For $\nu = 1$ in Fig. 5(b), there appear 4-fold degenerate zero-energy GSs at $\gamma = 0$, which are given by the products of Laughlin states; a large gap opens above these GSs, and it decreases more slowly for $\gamma < 0$ than for $\gamma > 0$ with increasing $|\gamma|$. Although the behaviors of the spectra are more complex for $\nu = 4/3$ and 2 in Fig. 5(c,d), we can see the emergence of energy gaps above the doubled CF states [around $\gamma = 0$ in (c)] and the BIQH state [around $\gamma = 1$ in (d)]. The gap above the $SU(3)_2$ state with 6-fold degeneracy at $\nu = 4/3$ is analyzed in more detail in Refs. [39, 40]. In Fig. 5(b,c,d), we can further find the occurrence of a phase separation for large γ through the replacement of the GS with an imbalanced state with $N_\uparrow \neq N_\downarrow$. The boundaries of phase separated regions in Fig. 1 are estimated in this way from Fig. 5(b,c,d).

D. Collapse of the gas for $\gamma < -\pi/4$

Similar to the case of antiparallel fields [60], a collapse of the gas occurs for $\gamma < -\pi/4$ owing to the dominance of an intercomponent attraction. As seen in Fig. 6, the GS energy $E_{\rm GS}(N)$ as a function of N is convex for $\gamma > -\pi/4$ and is concave for $\gamma < -\pi/4$. This indicates that the compressibility κ, which is inversely proportional to $\frac{d^2 E_{\rm GS}}{dN^2}$, changes the sign across $\gamma = -\pi/4$ (with a divergence $\kappa \to \pm\infty$ at the transition point). The state with $\kappa < 0$ for $\gamma < -\pi/4$ is thermodynamically unstable and spontaneously contracts, leading to a collapse of the gas (we note that within the LLL approximation, a genuine collapse with a divergence in the density occurs only in the thermodynamic limit, as commented in Ref. [60]).

III. INTERCOMPONENT ENTANGLEMENT AND PSEUDOPOTENTIALS

The phase diagram in Fig. 1, which is determined in the preceding section, shows a remarkable dependence on the sign of the intercomponent coupling $g_{\uparrow\downarrow}$. While doubled QH states are robust for $g_{\uparrow\downarrow} < 0$, they are destabilized for moderate $g_{\uparrow\downarrow}/g > 0$, and a variety of spin-singlet QH states with high intercomponent entanglement emerge for $g_{\uparrow\downarrow}/g \approx 1$. Interestingly, a qualitatively opposite dependence on the sign of $g_{\uparrow\downarrow}$ has been found in two-component Bose gases in antiparallel fields [60]: in this case, the products of a pair of QH states are more stable for $g_{\uparrow\downarrow} > 0$ than for $g_{\uparrow\downarrow} < 0$. In this section, we present an interpretation of these results in light of pseudopotentials on a spherical geometry.

The pseudopotential representation of interactions is introduced in the following way [57, 58]. In a scattering process of two particles on a sphere, their total angular momentum is conserved because of the spherical spacial symmetry. The two-body interaction Hamiltonian (2) can therefore be decomposed as

$$H_{\rm int} = \frac{1}{2} \sum_{\alpha,\beta=\uparrow,\downarrow} \sum_{J=0}^{2S} V_J^{\alpha\beta} \sum_{M=-J}^{J} A_{JM}^{\alpha\beta\dagger} A_{JM}^{\alpha\beta}. \qquad (7)$$

Here, we have introduced the pair creation operator

$$A_{JM}^{\alpha\beta\dagger} = \sum_{m_1+m_2=M} b_{m_1\alpha}^\dagger b_{m_2\beta}^\dagger \langle S, m_1; S, m_2 | J, M\rangle, \qquad (8)$$

where $b_{m\alpha}^\dagger$ is the bosonic creation operator for the pseudospin state α and the m-th orbital in the LLL, and $\langle S, m_1; S, m_2 | J, M\rangle$ is the Clebsch-Gordan coefficient. We note that $A_{JM}^{\alpha\alpha} = 0$ when $S - J$ is odd, owing to the bosonic statistics. The coefficient $V_J^{\alpha\beta}$ describes the interaction energy of two particles with pseudospin states α and β in the total angular momentum J, and is called the pseudopotential. The expansion (7) is analogous to the decomposition of an interaction between spinor atoms in terms of the total spin magnitude [73, 74].

In the case of two-component gases in parallel fields, the pseudopotentials are calculated to be

$$V_J^{\alpha\beta} = \delta_{J,2S} \frac{g_{\alpha\beta}}{4\pi\ell^2} \frac{(2S+1)^2}{S(4S+1)}. \qquad (9)$$

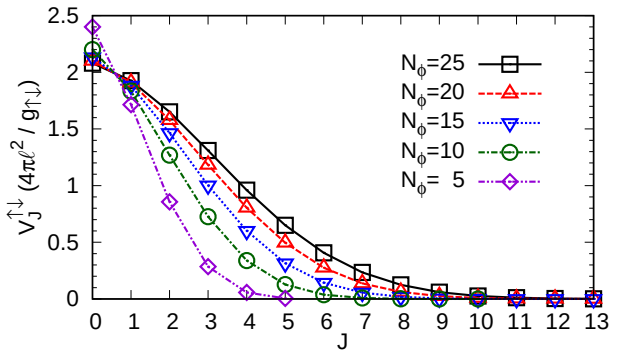

FIG. 7: (color online) Intercomponent pseudopotential (10) as a function of the total angular momentum J of two particles in antiparallel fields on a sphere.

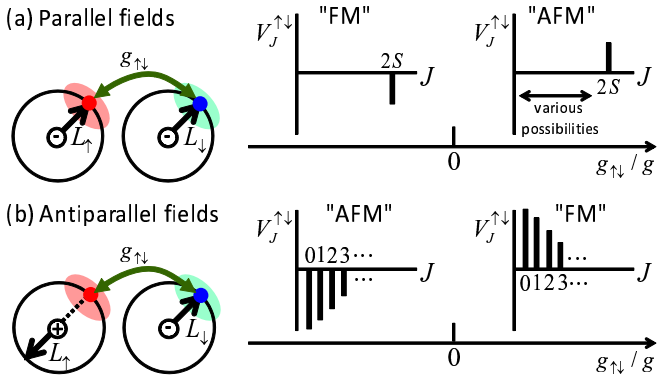

FIG. 8: (color online) Schematic pictures of modified angular momenta $\boldsymbol{L}_{\uparrow,\downarrow}$ (left) and the intercomponent pseudopotential $V_J^{\uparrow\downarrow}$ (right) on a spherical geometry. The sign at the center of a sphere indicates the sign of the magnetic monopole charge in units of $2\pi\hbar/q$ for each component. See Eqs. (9) and (10) for the expressions of $V_J^{\uparrow\downarrow}$ and Fig. 7 for the plot of Eq. (10). In the case of (a) parallel fields, a repulsive (attractive) coupling $g_{\uparrow\downarrow} > 0$ ($g_{\uparrow\downarrow} < 0$) between $\uparrow$ and $\downarrow$ particles can be viewed as an "AFM" ("FM") interaction between their angular momenta. In the case of (b) antiparallel fields, in contrast, an intercomponent repulsion (attraction) can be viewed as a "FM" ("AFM") interaction between the angular momenta. The intercomponent coupling of an "AFM" type is expected to produce higher entanglement between the two components than the one of a "FM" type. An intercomponent repulsion $g_{\uparrow\downarrow} > 0$ in (a) has a particularly large flexibility in the way of forming entanglement between the two components, which qualitatively explains why a variety of spin-singlet QH states emerge for $g_{\uparrow\downarrow} \approx g$.

As seen in this expression, $V_J^{\alpha\beta}$ is nonzero only when J takes the maximal value $2S$. In the case of two-component gases in antiparallel fields, the intracomponent pseudopotentials $V_J^{\alpha\alpha}$ are given by the same form as Eq. (9) while the intercomponent one is given by

$$V_J^{\uparrow\downarrow} = \frac{g_{\uparrow\downarrow}}{4\pi\ell^2} \frac{[(2S+1)!]^2}{S(2S-J)!(2S+J+1)!}. \qquad (10)$$

See Appendix B for the derivation of Eqs. (9) and (10). Equation (10) is plotted in Fig. 7. As seen in this figure, $V_J^{\uparrow\downarrow}$ in units of $g_{\uparrow\downarrow}/(4\pi\ell^2)$ takes the maximum of around 2 for $J = 0$, and decreases monotonically with increasing J; furthermore, with increasing $N_\phi = 2S$, the decrease of $V_J^{\uparrow\downarrow}$ as a function of J becomes slower.

Figure 8 summarizes the behaviors of the intercomponent pseudopotential $V_J^{\uparrow\downarrow}$ for parallel and antiparallel fields (right) and presents their interpretations in terms of angular momenta (left). In the case of (a) parallel fields, a particle is located around the direction of its angular momentum $\langle \boldsymbol{L}_\alpha \rangle$ [57, 58]. In this case, a repulsive (attractive) interaction between $\uparrow$ and $\downarrow$ particles can be viewed as an "antiferromagnetic (AFM)" ["ferromagnetic (FM)"] interaction between their angular momenta $\boldsymbol{L}_{\uparrow,\downarrow}$. This is consistent with the behavior of $V_J^{\uparrow\downarrow}$ in Eq. (9), which disfavors (favors) the maximal total angular momentum $J = 2S$ for $g_{\uparrow\downarrow} > 0$ ($g_{\uparrow\downarrow} < 0$). In the case of (b) antiparallel fields, in contrast, a pseudospin-$\uparrow$ particle is located around the direction of $-\langle \boldsymbol{L}_\uparrow \rangle$. Thus, a repulsive (attractive) interaction between $\uparrow$ and $\downarrow$ particles can be viewed as a "FM" ("AFM") interaction between their angular momenta $\boldsymbol{L}_{\uparrow,\downarrow}$. This is consistent with Eq. (10), which disfavors (favors) states with small J for $g_{\uparrow\downarrow} > 0$ ($g_{\uparrow\downarrow} < 0$).

Now the phase diagrams in the cases of parallel and antiparallel fields can be understood as follows. In the absence of an intercomponent coupling $g_{\uparrow\downarrow}$, the intracomponent pseudopotential $V_J^{\alpha\alpha}$ having an "AFM" nature leads to the formation of QH states in each component. Such QH states reside in the singlet sector ($L = 0$) of the total angular momentum, and thus are highly entangled with respect to angular momenta of particles in each component. In the case of parallel (antiparallel) fields, an intercomponent attraction $g_{\uparrow\downarrow} < 0$ (repulsion $g_{\uparrow\downarrow} > 0$) introduces a "FM" interaction between angular momenta of particles in different components. Since such an interaction favors the formation of product states such as $|J = 2S, M = 2S\rangle = |S, S; S, S\rangle$ for two particles in different components, it is not likely to produce high entanglement between the components. In contrast, an intercomponent repulsion $g_{\uparrow\downarrow} > 0$ (attraction $g_{\uparrow\downarrow} < 0$) in the case of parallel (antiparallel) fields has an "AFM" nature and is expected to produce high entanglement between the components. Because of the monogamy of entanglement [76], the entanglement formation between the components leads to the destruction of entanglement in each component. Thus, the doubled QH states are less stable for such an interaction. As shown in Fig. 8, an intercomponent repulsion $g_{\uparrow\downarrow} > 0$ in the case of (a) parallel fields favors all the two-body states with $J \neq 2S$ equally, and thus has a large flexibility in the way of forming entanglement between the components. This qualitatively explains why a rich variety of spin-singlet QH states emerge for $g_{\uparrow\downarrow} \approx g$. Meanwhile, an intercom-

ponent attraction $g_{\uparrow\downarrow} < 0$ in the case of (b) antiparallel fields favors two-body states with small J rather selectively, and is likely to lead to simpler physics. In particular, when $g_{\uparrow\downarrow} = -g < 0$, the GS is given exactly by the singlet-pairing state $(A_{00}^{\uparrow\downarrow\dagger})^{N/2}|\mathrm{vac}\rangle$ for all even N [60]. We note that the formation of larger entanglement for AFM intercomponent couplings than for FM ones is also found in the quantum GSs of a binary mixture of spinor Bose-Einstein condensates [75]. Generalization of the present argument to other geometries such as a disc and a torus remains as an important open problem.

IV. SUMMARY AND OUTLOOK

In this paper, we have determined the QH phase diagram of two-component Bose gases in a synthetic magnetic field as shown in Fig. 1. We have revealed a remarkable dependence on the sign of the intercomponent coupling $g_{\uparrow\downarrow}$: while the product states of a pair of QH states are robust for $g_{\uparrow\downarrow} < 0$, they are destabilized for moderate $g_{\uparrow\downarrow}/g$ and a variety of spin-singlet QH states with high intercomponent entanglement emerge for $g_{\uparrow\downarrow} \approx g$. We interpret these results in light of pseudopotentials on a sphere. The pseudopotential approach also explains recent numerical results in two-component Bose gases in antiparallel fields [60] where a qualitatively opposite dependence on the sign of $g_{\uparrow\downarrow}$ is found.

It is interesting to ask whether the relationship between the cases of parallel and antiparallel fields revealed in the present study and Ref. [60] applies to more general systems. Repellin *et al.* [64] have found in lattice models that two coupled bosonic Laughlin states with opposite chiralities (i.e., fractional quantum spin Hall states [63]) are more robust than the ones with the same chiralities for an intercomponent repulsion; the case of an intercomponent attraction has yet to be analyzed. The stability of fractional quantum spin Hall states against an intercomponent repulsion has also been studied in time-reversal-invariant models of spin-$\frac{1}{2}$ fermions in lattices [77, 78] and continuum [79], and in a model of strained graphene [80]; it is intriguing to compare these systems with their time-reversal-breaking counterparts. Further studies in these directions would strengthen the connection between two active research fields, multicomponent QH systems [81] and a strongly correlated regime of spin Hall systems [63].

This work was supported by KAKENHI Grant Nos. JP25800225 and JP26287088 from the Japan Society for the Promotion of Science, a Grant-in-Aid for Scientific Research on Innovative Areas "Topological Materials Science" (KAKENHI Grant No. JP15H05855), the Photon Frontier Network Program from MEXT of Japan, and the Matsuo Foundation.

Appendix A: Quantum Hall wave functions

Here we summarize QH wave functions discussed in this paper.

Let us first review the case of scalar Bose gases. We consider a disc geometry, where the LLL orbitals are given by $\psi_m(z) \propto z^m \exp[-|z|^2/(4\ell^2)]$ $(m = 0, 1, \ldots, N_\phi)$ with $z = x + iy$ being a complex coordinate. In this geometry, a general many-body wave function has a form

$$\Psi(\{z_i\}) = \tilde{\Psi}(\{z_i\}) e^{-\sum_j |z_j|^2/(4\ell^2)}, \tag{A1}$$

where $\tilde{\Psi}(\{z_i\})$ is a symmetric polynomial of the coordinates $\{z_j\}$ of the N bosons. In the following, we use either Ψ or $\tilde{\Psi}$ to represent each QH wave function.

The Laughlin wave function [25] at the filling factor $\nu = 1/2$ is given by

$$\tilde{\Psi}^{\mathrm{Laughlin}} = \prod_{i<j} (z_i - z_j)^2. \tag{A2}$$

This is an exact zero-energy GS for a repulsive contact interaction as the amplitude of this wave function vanishes when any two particles come to the same point [26]. Using this wave function, one can construct the Read-Rezayi series of states [32] at $\nu = k/2$ $(k = 1, 2, \ldots)$, which has an $\mathrm{SU}(2)_k$ symmetry. Their wave functions can be represented as [82]

$$\tilde{\Psi}^{\mathrm{SU}(2)_k} = \mathcal{S}_{\mathrm{group}} \prod_{\mathrm{group}} \tilde{\Psi}^{\mathrm{Laughlin}}. \tag{A3}$$

Here, the N bosons are first partitioned into k groups with equal populations. For each group, we write a Laughlin factor $\tilde{\Psi}^{\mathrm{Laughlin}}$, and then such factors are multiplied together. Finally, we apply the symmetrization operation $\mathcal{S}_{\mathrm{group}}$ over all different ways of dividing the particles into k groups. For $k = 1$, Eq. (A3) clearly gives the Laughlin wave function (A2); for $k = 2$, Eq. (A3) is equivalent to the Moore-Read ("Pfaffian") wave function [30]

$$\tilde{\Psi}^{\mathrm{MR}} = \mathrm{Pf}\left(\frac{1}{z_i - z_j}\right) \prod_{i<j} (z_i - z_j). \tag{A4}$$

The $\mathrm{SU}(2)_k$ states with $k \geq 2$ exhibit excitations obeying non-Abelian statistics. The wave function (A3) is a unique zero-energy GS of a Hamiltonian consisting of a $(k+1)$-body interaction

$$H_k = \sum_{i_1 < \cdots < i_{k+1}} \delta(z_{i_1} - z_{i_2}) \cdots \delta(z_{i_k} - z_{i_{k+1}}). \tag{A5}$$

For scalar bosons interacting via a repulsive contact interaction, the $\mathrm{SU}(2)_k$ wave functions (A3) have been found to give good approximations to the GSs for small k [28, 31, 83]. On a sphere, the candidate wave functions can be obtained through the replacement $z_i - z_j \to$

$u_i v_j - v_i u_j$ in the above wave functions; since the largest power of z_1 in Eq. (A3) is given by $N_\phi = 2(N/k-1)$, these wave functions have the shift $\delta = 2$. On a torus, the $\mathrm{SU}(2)_k$ state exhibits topological GS degeneracy of $k+1$.

Another important series of QH states are Jain's CF states [27, 28] at $\nu = \frac{p}{p+1}$ ($p = 1, 2, \dots$); at these filling factors, binding of a unit flux to each boson leads to the integer QH states of CFs at the effective filling factors $\nu^* = p$. The corresponding wave functions are given by [27, 29, 84]

$$\Psi^{\mathrm{CF}}_{\frac{p}{p+1}}(\{z_i\}) = \mathcal{P}_{\mathrm{LLL}} J(\{z_i\}) \Phi_p(\{z_i\}), \tag{A6}$$

where $J(\{z_i\}) = \prod_{i<j}(z_i - z_j)$ is the Jastrow factor, $\Phi_p(\{z_i\})$ is the Slater determinant obtained by filling exactly p Landau levels, and $\mathcal{P}_{\mathrm{LLL}}$ is the projection onto the LLL manifold. For $p = 1$, this wave function reproduces the Laughlin wave function (A2). For $p = 2$ and 3, the wave function (A6) (with a slight modification of the projection for technical convenience) has been confirmed to give good approximations to the GSs for a two-body contact interaction in numerical analyses of finite-size systems [29].

Let us now turn to the case of two-component Bose gases studied in this paper. Since the QH states for small $g_{\uparrow\downarrow}/g$ are simply the products of two QH states in the scalar case, we here focus on the spin-singlet QH states appearing for $g_{\uparrow\downarrow} \approx g$. The Halperin (221) wave function [35, 36] at the total filling factor $\nu = 1/3 + 1/3$ is given by

$$\tilde{\Psi}^{221} = \prod_{i<j}(z_i^\uparrow - z_j^\uparrow)^2 \prod_{i<j}(z_i^\downarrow - z_j^\downarrow)^2 \prod_{i,j}(z_i^\uparrow - z_j^\downarrow). \tag{A7}$$

The contact interactions in Eq. (2) vanish for this wave function, and therefore Eq. (A7) is an exact zero-energy GS for arbitrary $g_{\uparrow\downarrow} \geq 0$ and $g \geq 0$ [36]. Using this wave function, one can construct a series of non-Abelian spin-singlet states at $\nu = k/3 + k/3$ with integer k [37], which have an $\mathrm{SU}(3)_k$ symmetry (more generally, the $\mathrm{SU}(n+1)_k$ states at $\nu = nk/(n+1)$ can be constructed for n-component Bose gases [85]). On a disc, their wave functions are written as

$$\tilde{\Psi}^{SU(3)_k} = \mathcal{S}_{\mathrm{group}} \prod_{\mathrm{group}} \tilde{\Psi}^{221}. \tag{A8}$$

Here, as in the Read-Rezayi wave functions (A3), N bosons are first partitioned into k groups (each with $N/(2k)$ particles in each spin state $\uparrow, \downarrow$), a Halperin $\tilde{\Psi}^{221}$ factor is constructed in each group, and then the symmetrization $\mathcal{S}_{\mathrm{group}}$ is taken. The $\mathrm{SU}(3)_k$ states with $k \geq 2$ exhibit excitations obeying non-Abelian statistics. The wave function (A8) is again a unique zero-energy GS for a $(k+1)$-body interaction (A5) for two components on a disc. Since the largest power of $z_1^\uparrow$ in Eq. (A8) is given by $N_\phi = 2\left(\frac{N}{2k} - 1\right) + \frac{N}{2k}$, these wave functions have the shift $\delta = 2$ on a sphere. On a torus, the $\mathrm{SU}(3)_k$ state exhibits topological GS degeneracy of $(k+1)(k+2)/2$. For two-body contact interactions (2) with $g_{\uparrow\downarrow} \approx g$, the $\mathrm{SU}(2)_2$ state has been found to give a good approximation to the GS at $\nu = 4/3$ [38–40].

One can further introduce a series of CFSS states [43, 86] at $\nu = \frac{p}{2p\pm1} + \frac{p}{2p\pm1}$ ($p = 1, 2, \dots$); here, binding of a unit flux with each boson leads to the integer QH states of CFs at $\nu^* = \pm(p+p)$. The corresponding wave functions are given by

$$\Psi^{\mathrm{CFSS}}_{\frac{2p}{2p\pm1}}(\{z_i\}) = \mathcal{P}_{\mathrm{LLL}} J(\{z_i\}) \Phi_{\pm p}(\{z_i^\uparrow\}) \Phi_{\pm p}(\{z_i^\downarrow\}), \tag{A9}$$

where $J(\{z_i\})$ is the Jastrow factor for all the particles, and $\Phi_{-p}(\{z_i^\alpha\}) = \Phi_p^*(\{z_i^\alpha\})$. For $\nu = 2/(2+1) = 2/3$, this wave function reproduces the Halperin (221) wave function. For $\nu = 2/(2-1) = 2$, the wave function (A9) gives the BIQH wave function [41], which is a good approximation to the GS for two-body contact interactions (2) with $g_{\uparrow\downarrow} = g$ [43]. The BIQH state is particularly intriguing as it is a symmetry-protected topological state of bosons in two dimensions [87, 88] and exhibits counterpropagating charge and spin modes at the edge [41], as numerically demonstrated in Refs. [42, 43]. Indication for the appearance of the $\nu = 4/(4\pm1)$ CFSS states has also been found in Ref. [43] (see purple double dotted lines in Fig. 2). However, the CFSS state at $\nu = 4/3$ competes with the $\mathrm{SU}(3)_2$ state, and this competition has been analyzed in Refs [42, 43].

Indication of gapped states at $\nu = 4$ and 6 has been found in Ref. [42] (see blue dotted lines in Fig. 2). While we have not achieved appropriate characterizations of these states, the real-space entanglement spectrum of the $\nu = 4$ state reveals a counterpropagating nature of edge modes, suggesting similarities with the BIQH state at $\nu = 2$.

Appendix B: Pseudopotentials for antiparallel fields

Here we describe the calculation of pseudopotentials for pseudospin-$\frac{1}{2}$ Bose gases in antiparallel magnetic fields on a spherical geometry. Such systems have been studied previously [60–62], and we basically take the same notations as in Ref. [60]. A related calculation of pseudopotentials for two-species Dirac fermions in antiparallel fields is presented in Ref. [89].

We introduce the polar coordinates (r, θ, ϕ) and associated unit vectors $\boldsymbol{e}_r, \boldsymbol{e}_\theta, \boldsymbol{e}_\phi$. We place a pseudospin-dependent magnetic monopole of charge $\epsilon_\alpha N_\phi (2\pi\hbar/q)$ with integer $N_\phi \equiv 2S$ at the center of the sphere, where $\epsilon_\uparrow = +1$ and $\epsilon_\downarrow = -1$. This monopole produce a magnetic field $\epsilon_\alpha B$ on the sphere of radius $R = \ell\sqrt{S}$. For this problem, it is useful to introduce the modified angular momentum

$$\boldsymbol{L}_\alpha = \boldsymbol{r} \times \left(\boldsymbol{p} + \epsilon_\alpha \frac{\hbar S \cot\theta}{r} \boldsymbol{e}_\phi \right) - \epsilon_\alpha \hbar S \boldsymbol{e}_r, \tag{B1}$$

which obeys the standard algebra of an angular momentum. The LLL for a pseudospin-α particle on the sphere

corresponds to the subspace in which $\boldsymbol{L}_\alpha$ has the magnitude of S. The single-particle orbitals in the LLL are given by [57, 58, 60]

$$\psi_{m\uparrow}(\boldsymbol{r}) = \frac{\bar{v}^{S+m}(-\bar{u})^{S-m}}{\sqrt{4\pi R^2 \mathcal{N}_{S,-m}}},\ \psi_{m\downarrow}(\boldsymbol{r}) = \frac{u^{S+m}v^{S-m}}{\sqrt{4\pi R^2 \mathcal{N}_{Sm}}}, \tag{B2}$$

for the pseudospin states $\uparrow$ and $\downarrow$, respectively. Here, $m \in \{-S, -S+1, \ldots, S\}$ is the eigenvalue of $L^z_\alpha/\hbar$, $\boldsymbol{r}$ is constrained to the surface of the sphere ($\boldsymbol{r} = R\boldsymbol{e}_r$), and (u, v) and $(\bar{u}, \bar{v})$ are the spinor coordinates (3) and their complex conjugates. The normalization factor $\mathcal{N}_{Sm}$ is given by

$$\mathcal{N}_{Sm} = \int \frac{d^2\boldsymbol{r}}{4\pi R^2}|u|^{2(S+m)}|v|^{2(S-m)} = \frac{(S+m)!(S-m)!}{(2S+1)!}. \tag{B3}$$

It is worth noting that the orbital $\psi_{m\alpha}$ has the average location

$$\langle\psi_{m\alpha}|\cos\theta|\psi_{m\alpha}\rangle = \int d^2\boldsymbol{r}\cos\theta|\psi_{m\alpha}(\boldsymbol{r})|^2 = \frac{-\epsilon_\alpha m}{S+1}. \tag{B4}$$

In particular, the $m = S$ state for $\alpha = \uparrow$ ($\downarrow$) is localized around the south (north) pole of a sphere. This suggests that a pseudospin-α particle in the LLL is in general located around the direction of $-\epsilon_\alpha\langle\boldsymbol{L}_\alpha\rangle$, as schematically shown in Fig. 8(b).

The pseudopotentials are defined as the eigenenergies of the interaction Hamiltonian (2) for two-body eigenstates. Such two-body eigenstates can be calculated through the angular-momentum coupling of Eq. (B2) as

$$\Phi^{\alpha\beta}_{JM}(\boldsymbol{r}_1, \boldsymbol{r}_2) = \sum_{m_1+m_2=M} \psi_{m_1\alpha}(\boldsymbol{r}_1)\psi_{m_2\beta}(\boldsymbol{r}_2) \times\langle S, m_1; S, m_2|J, M\rangle, \tag{B5}$$

where $\alpha, \beta = \uparrow, \downarrow$. For a general interaction potential $V_{\alpha\beta}(\boldsymbol{r})$, the pseudopotentials are given by

$$V^{\alpha\beta}_J = \int d^2\boldsymbol{r}_1 d^2\boldsymbol{r}_2 V_{\alpha\beta}(\boldsymbol{r}_1 - \boldsymbol{r}_2)|\Phi^{\alpha\beta}_{JM}(\boldsymbol{r}_1, \boldsymbol{r}_2)|^2. \tag{B6}$$

Since the right-hand side does not depend on M, it is sufficient to consider the case of $M = J$. Furthermore, since $V_{\uparrow\uparrow} = V_{\downarrow\downarrow}$ and $V_{\uparrow\downarrow} = V_{\downarrow\uparrow}$ in the case of our interest, we can focus on the cases of $(\alpha, \beta) = (\downarrow, \downarrow)$ and $(\uparrow, \downarrow)$. In these cases, using the expressions of the Clebsch-Gordan coefficients, the two-body eigenstates (B5) are calculated to be [57, 58, 89]

$$\Phi^{\downarrow\downarrow}_{JJ}(\boldsymbol{r}_1, \boldsymbol{r}_2) = \frac{(u_1v_2 - v_1u_2)^{2S-J}(u_1u_2)^J}{4\pi R^2\mathcal{M}^{1/2}_{SJ}}, \tag{B7a}$$

$$\Phi^{\uparrow\downarrow}_{JJ}(\boldsymbol{r}_1, \boldsymbol{r}_2) = \frac{(\bar{v}_1v_2 + \bar{u}_1u_2)^{2S-J}(\bar{v}_1u_2)^J}{4\pi R^2\mathcal{M}^{1/2}_{SJ}}, \tag{B7b}$$

where we introduce the spinor coordinates (u_i, v_i) for $\boldsymbol{r}_i$ $(i = 1, 2)$ as in Eq. (3), and the normalization factor $\mathcal{M}_{SJ}$ is given by

$$\mathcal{M}_{SJ} = \mathcal{N}_{J,0}\frac{(2S-J)!(2S+J+1)!}{[(2S+1)!]^2}. \tag{B8}$$

We now focus on the case of contact interactions $V_{\alpha\beta}(\boldsymbol{r}) = g_{\alpha\beta}\delta(\boldsymbol{r})$ with $g_{\uparrow\uparrow} = g_{\downarrow\downarrow} = g > 0$. By substituting Eq. (B7a) into Eq. (B6), the intracomponent pseudopotential is calculated as

$$V^{\downarrow\downarrow}_J = g\int d^2\boldsymbol{r}|\Phi^{\downarrow\downarrow}_{JJ}(\boldsymbol{r}, \boldsymbol{r})|^2 = V^{\downarrow\downarrow}_{2S}\delta_{J,2S}, \tag{B9}$$

where

$$V^{\downarrow\downarrow}_{2S} = \frac{g\mathcal{N}_{2S,2S}}{4\pi R^2\mathcal{M}_{S,2S}} = \frac{g}{4\pi\ell^2}\frac{(2S+1)^2}{S(4S+1)}. \tag{B10}$$

In the limit $S \to \infty$, V_{2S} converges to $g/(4\pi\ell^2)$, which coincides with the pseudopotential for zero relative angular momentum in a single-component gas on the disk geometry [6]. Similarly, by substituting Eq. (B7b) into Eq. (B6), the intercomponent pseudopotential is calculated as

$$V^{\uparrow\downarrow}_J = \frac{g_{\uparrow\downarrow}\mathcal{N}_{J,0}}{4\pi R^2\mathcal{M}_{SJ}} = \frac{g_{\uparrow\downarrow}}{4\pi\ell^2}\frac{[(2S+1)!]^2}{S(2S-J)!(2S+J+1)!}, \tag{B11}$$

which gives Eq. (10).

[1] J. Dalibard, F. Gerbier, G. Juzeliūnas, and P. Öhberg, Rev. Mod. Phys. **83**, 1523 (2011).
[2] N. Goldman, G. Juzeliūnas, P. Öhberg, I. B. Spielman, Rep. Prog. Phys. **77**, 126401 (2014).
[3] K. W. Madison, F. Chevy, W. Wohlleben, and J. Dalibard, Phys. Rev. Lett. **84**, 806 (2000).
[4] J. R. Abo-Shaeer, C. Raman, J. M. Vogels, and W. Ketterle, Science **292**, 476 (2001).
[5] V. Schweikhard, I. Coddington, P. Engels, V. P. Mogendorff, and E. A. Cornell, Phys. Rev. Lett. **92**, 040404 (2004).
[6] N. R. Cooper, Adv. Phys. **57**, 539 (2008).
[7] Y.-J. Lin, R. L. Compton, K. Jinménez-García, J. V. Porto, and I. B. Spielman, Nature **462**, 628 (2009).
[8] M. Aidelsburger, M. Atala, M. Lohse, J. T. Barreiro, B. Paredes, and I. Bloch, Phys. Rev. Lett. **111**, 185301 (2013).
[9] H. Miyake, G. A. Siviloglou, C. J. Kennedy, W. C. Bur-

ton, and W. Ketterle, Phys. Rev. Lett. **111**, 185302 (2013).
[10] M. Aidelsburger, M. Lohse, C. Schweizer, M. Atala, J. T. Barreiro, S. Nascimbene, N. R. Cooper, I. Bloch, and N. Goldman, Nat. Phys. **11**, 162 (2015).
[11] A. Celi, P. Massignan, J. Ruseckas, N. Goldman, I. B. Spielman, G. Juzeliūnas, and M. Lewenstein, Phys. Rev. Lett. **112**, 043001 (2014).
[12] M. Mancini, G. Pagano, G. Cappellini, L. Livi, M. Rider, J. Catani, C. Sias, P. Zoller, M. Inguscio, M. Dalmonte, and L. Fallani, Science **349**, 1510 (2015).
[13] B. K. Stuhl, H.-I Lu, L. M. Aycock, D. Genkina, and I. B. Spielman, Science **349**, 1514 (2015).
[14] D. S. Hall, M. R. Matthews, J. R. Ensher, C.E. Wieman, and E. A. Cornell, Phys. Rev. Lett. **81**, 1539 (1998).
[15] V. Schweikhard, I. Coddington, P. Engels, S. Tung, and E. A. Cornell, Phys. Rev. Lett. **93**, 210403 (2004).
[16] Y.-J. Lin, K. Jiménez-Garcia, and I. B. Spielman, Nature **471**, 83 (2011).
[17] P. Wang, Z.-Q. Yu, Z. Fu, J. Miao, L. Huang, S. Chai, H. Zhai, and J. Zhang, Phys. Rev. Lett. **109**, 095301 (2012).
[18] L. Huang, Z. Meng, P. Wang, P. Peng, S.-L. Zhang, L. Chen, D. Li, Q. Zhou, and J. Zhang, Nat. Phys. **12**, 540 (2016);
[19] Z. Wu, L. Zhang, W. Sun, X.-T. Xu, B.-Z. Wang, S.-C. Ji, Y. Deng, S. Chen, X.-J. Liu, J.-W. Pan, Science **354**, 83 (2016).
[20] H. Zhai, Int. J. Mod. Phys. B **26**, 1230001 (2012).
[21] V. Galitski and I. B. Spielman, Nature **494**, 49 (2013).
[22] M. C. Beeler, R. A. Williams, K. Jiménez-Garcia, L. J. LeBlanc, A. R. Perry, and I. B. Spielman, Nature **498**, 201 (2013).
[23] I. Bloch, J. Dalibard, and S. Nascimbene, Nat. Phys. **8**, 267 (2012).
[24] N. Goldman, J. C. Budich, and P. Zoller, Nat. Phys. **12**, 639 (2016).
[25] R. B. Laughlin, Phys. Rev. Lett. **50**, 1395 (1983).
[26] N. K. Wilkin, J. M. F. Gunn, and R. A. Smith, Phys. Rev. Lett. **80**, 2265 (1998).
[27] J. K. Jain, Phys. Rev. Lett. **63**, 199 (1989); Phys. Rev. B **41**, 7653 (1990).
[28] N. Regnault and Th. Jolicoeur, Phys. Rev. Lett. **91**, 030402 (2003); Phys. Rev. B **69**, 235309 (2004).
[29] C.-C. Chang, N. Regnault, Th. Jolicoeur, and J. K. Jain, Phys. Rev. A **72**, 013611 (2005).
[30] G. Moore and N. Read, Nucl. Phys. **B360**, 362 (1991).
[31] N. R. Cooper, N. K. Wilkin, and J. M. F. Gunn, Phys. Rev. Lett. **87**, 120405 (2001).
[32] N. Read and E. H. Rezayi, Phys. Rev. B **59**, 8084 (1999).
[33] E. J. Mueller and T.-L. Ho, Phys. Rev. Lett. **88**, 180403 (2002).
[34] K. Kasamatsu, M. Tsubota, and M. Ueda, Phys. Rev. Lett. **91**, 150406 (2003); Int. J. Mod. Phys. B **19**, 1835 (2005).
[35] B. Halperin, Helv. Phys. Acta **56**, 75 (1983).
[36] B. Paredes, P. Zoller, and J. I. Cirac, Phys. Rev. A **66**, 033609 (2002).
[37] E. Ardonne and K. Schoutens, Phys. Rev. Lett. **82**, 5096 (1999); E. Ardonne, N. Read, and E. Rezayi, and K. Schoutens, Nucl. Phys. B **607**, 549 (2001).
[38] L. Hormozi, G. Möller, and S. H. Simon, Phys. Rev. Lett. **108**, 256809 (2012).
[39] T. Graß, B. Juliá-Díaz, N. Barberán, and M. Lewenstein, Phys. Rev. A **86**, 021603 (R) (2012).
[40] S. Furukawa and M. Ueda, Phys. Rev. A **86**, 031604 (R) (2012).
[41] T. Senthil and M. Levin, Phys. Rev. Lett. **110**, 046801 (2013).
[42] S. Furukawa and M. Ueda, Phys. Rev. Lett. **111**, 090401 (2013).
[43] Y.-H. Wu and J. K. Jain, Phys. Rev. B **87**, 245123 (2013).
[44] N. Regnault and T. Senthil, Phys. Rev. B **88**, 161106 (2013).
[45] T. Graß, D. Raventós, M. Lewenstein, and B. Juliá-Díaz, Phys. Rev. B **89**, 045114 (2014).
[46] M. Nakagawa and S. Furukawa, arXiv:1701.01127.
[47] M. Barkeshli and X.-L. Qi, Phys. Rev. X **2**, 031013 (2012).
[48] Y.-F. Wang, H. Yao, C.-D. Gong, and D. N. Sheng, Phys. Rev. B **86**, 201101 (R) (2012).
[49] S. Yang, Z.-C. Gu, K. Sun, and S. Das Sarma, Phys. Rev. B **86**, 241112 (2012).
[50] Z. Liu, E. J. Bergholtz, H. Fan, and A. M. Läuchli, Phys. Rev. Lett. **109**, 186805 (2012).
[51] A. Sterdyniak, C. Repellin, B. Andrei Bernevig, and N. Regnault, Phys. Rev. B **87**, 205137 (2013).
[52] Y.-L. Wu, N. Regnault, and B. A. Bernevig, Phys. Rev. Lett. **110**, 106802 (2013); Y.-H. Wu, J. K. Jain, and K. Sun, Phys. Rev. B **91**, 041119 (2015).
[53] A. Sterdyniak, B. A. Bernevig, N. R. Cooper, and N. Regnault, Phys. Rev. B **91**, 035115 (2015); A. Sterdyniak, N. R. Cooper, and N. Regnault, Phys. Rev. Lett. **115**, 116802 (2015).
[54] T.-S. Zeng, W. Zhu, and D. N. Sheng, Phys. Rev. B **93**, 195121 (2016).
[55] Y.-C. He, S. Bhattacharjee, R. Moessner, and F. Pollmann, Phys. Rev. Lett. **115**, 116803 (2015); Y. Fuji, Y.-C. He, S. Bhattacharjee, and F. Pollmann, Phys. Rev. B **93**, 195143 (2016).
[56] Y.-H. Wu and J. K. Jain, Phys. Rev. A **91**, 063623 (2015).
[57] F. D. M. Haldane, Phys. Rev. Lett. **51**, 605 (1983)
[58] G. Fano, F. Ortolani, and E. Colombo, Phys. Rev. B **34**, 2670 (1986).
[59] Z. Liu, A. Vaezi, C. Repellin, and N. Regnault, Phys. Rev. B **93**, 085115 (2016).
[60] S. Furukawa and M. Ueda, Phys. Rev. A **90**, 033602 (2014).
[61] X.-J. Liu, X. Liu, L. C. Kwek, and C. H. Oh, Phys. Rev. B **79**, 165301 (2009).
[62] O. Fialko, J. Brand, and U. Zülicke, New J. Phys. **16**, 025006 (2014).
[63] B. A. Bernevig and S.-C. Zhang, Phys. Rev. Lett. **96**, 106802 (2006).
[64] C. Repellin, B. A. Bernevig, and N. Regnault, Phys. Rev. B **90**, 245401 (2014).
[65] D. Yoshioka, Phys. Rev. B **29**, 6833 (1984).
[66] F. D. M. Haldane, Phys. Rev. Lett. **55**, 2095 (1985).
[67] T. Graß, B. Juliá-Díaz, M. Burrello, and M. Lewenstein, J. Phys. B: At. Mol. Opt. Phys. **46**, 134006 (2013).
[68] Y.-H. Wu, and T. Shi, Phys. Rev. B **94**, 075103 (2016).
[69] W.-L. You, Y.-W. Li, and S.-J. Gu, Phys. Rev. E **76**, 022101 (2007).
[70] N. Shibata and D. Yoshioka, Phys. Rev. Lett. **86**, 5755 (2001).
[71] A. E. Feiguin, E. Rezayi, C. Nayak, and S. Das Sarma, Phys. Rev. Lett. **100**, 166803 (2008).
[72] D. L. Kovrizhin, Phys. Rev. B **81**, 125130 (2010).
[73] Y. Kawaguchi and M. Ueda, Phys. Rep. **520**, 253 (2012).

[74] B. Lian and S.-C. Zhang, Phys. Rev. B **89**, 041110 (2014). In this reference, a simulation of bosonic Laughlin states in the spin space of ultracold atoms is proposed.

[75] Z. F. Xu, R. Lü, and L. You, Phys. Rev. A **84**, 063634 (2012). The model studied in this reference is described by the Hamiltonian (7) with $S = 1$, $V_J^{\uparrow\uparrow} = C_1\beta_1 J(J+1)$, $V_J^{\downarrow\downarrow} = C_2\beta_2 J(J+1)$, and $V_J^{\uparrow\downarrow} = \frac{1}{4}C_{12}\beta J(J+1) + \frac{1}{6}C_{12}\gamma\delta_{J,0}$.

[76] V. Coffman, J. Kundu, and W. K. Wootters, Phys. Rev. A **61**, 052306 (2000).

[77] T. Neupert, L. Santos, S. Ryu, C. Chamon, and C. Mudry, Phys. Rev. B **84**, 165107 (2011).

[78] W. Li, D. N. Sheng, C. S. Ting, and Y. Chen, Phys. Rev. B **90**, 081102 (R) (2014).

[79] H. Chen and K. Yang, Phys. Rev. B **85**, 195113 (2012).

[80] P. Ghaemi, J. Cayssol, D. N. Sheng, and A. Vishwanath, Phys. Rev. Lett. **108**, 266801 (2012).

[81] A. H. MacDonald and S. M. Girvin in *Perspectives in Quantum Hall Effects*, edited by S. Das Sarma and A. Pinczuk (Wiley, New York, 1997)

[82] A. Cappelli, L. S. Georgiev, and I. T. Todorov, Nucl. Phys. **B599**, 499 (2001).

[83] N. Regnault and Th. Jolicoeur, Phys. Rev. B **76**, 235324 (2007).

[84] J. K. Jain and R. K. Kamilla, Int. J. Mod. Phys. B **11**, 2621 (1997); Phys. Rev. B **55**, R4895 (1997).

[85] J. W. Reijnders, F. J. M. van Lankvelt, K. Schoutens, and N. Read, Phys. Rev. Lett. **89**, 120401 (2002); Phys. Rev. A **69**, 023612 (2004).

[86] X. G. Wu, G. Dev, and J. K. Jain, Phys. Rev. Lett. **71**, 153 (1993); K. Park and J. K. Jain, Phys. Rev. Lett. **80**, 4237 (1998); Phys. Rev. Lett. **83**, 5543 (1999).

[87] X. Chen, Z.-C. Gu, Z.-X. Liu, and X.-G. Wen, Science **338**, 1604 (2012); Phys. Rev. B **87**, 155114 (2013).

[88] Y.-M. Lu and A. Vishwanath, Phys. Rev. B **86**, 125119 (2012).

[89] H. Fujita, Y. O. Nakagawa, Y. Ashida, and S. Furukawa, Phys. Rev. A **94**, 043641 (2016).